2019

A versatile route to fabricate single atom catalysts with high chemoselectivity

Xiaohui He
Sun Yat-sen University

Qian He
Sun Yat-sen University

Yuchen Deng
Peking University

Mi Peng
Peking University

Hongyu Chen
Sun Yat-sen University

See next page for additional authors

Publisher Citation

He, X., He, Q., Deng, Y., Peng, M., Chen, H., Zhang, Y., ... & Ge, B. (2019). A versatile route to fabricate single atom catalysts with high chemoselectivity and regioselectivity in hydrogenation. Nature communications, 10(1), 1-9.

Comments

This article was published in the journal *Nature Communications.* https://doi.org/10.1038/s41467-019-11619-6

Authors
Xiaohui He, Qian He, Yuchen Deng, Mi Peng, Hongyu Chen, Ying Zhang, Siyu Yao, Mengtao Zhang, Dequan Xiao, Ding Ma, Binghui Ge, and Hongbing Ji

nature COMMUNICATIONS

ARTICLE

https://doi.org/10.1038/s41467-019-11619-6 OPEN

A versatile route to fabricate single atom catalysts with high chemoselectivity and regioselectivity in hydrogenation

Xiaohui He[1,7], Qian He[1,7], Yuchen Deng[2,7], Mi Peng[2], Hongyu Chen[1], Ying Zhang[1], Siyu Yao[2], Mengtao Zhang[2], Dequan Xiao[3], Ding Ma[2], Binghui Ge[4,5] & Hongbing Ji[1,6]

Preparation of single atom catalysts (SACs) is of broad interest to materials scientists and chemists but remains a formidable challenge. Herein, we develop an efficient approach to synthesize SACs via a precursor-dilution strategy, in which metalloporphyrin (MTPP) with target metals are co-polymerized with diluents (tetraphenylporphyrin, TPP), followed by pyrolysis to N-doped porous carbon supported SACs (M_1/N-C). Twenty-four different SACs, including noble metals and non-noble metals, are successfully prepared. In addition, the synthesis of a series of catalysts with different surface atom densities, bi-metallic sites, and metal aggregation states are achieved. This approach shows remarkable adjustability and generality, providing sufficient freedom to design catalysts at atomic-scale and explore the unique catalytic properties of SACs. As an example, we show that the prepared Pt_1/N-C exhibits superior chemoselectivity and regioselectivity in hydrogenation. It only converts terminal alkynes to alkenes while keeping other reducible functional groups such as alkenyl, nitro group, and even internal alkyne intact.

[1] Fine Chemical Industry Research Institute, School of Chemistry, Sun Yat-sen University, Guangzhou 510275, China. [2] Beijing National Laboratory for Molecular Sciences, College of Chemistry and Molecular Engineering and College of Engineering, and BIC-ESAT, Peking University, Beijing 100871, China. [3] Center for Integrative Materials Discovery, Department of Chemistry and Chemical Engineering, University of New Haven, 300 Boston Post Road, West Haven, CT 06516, USA. [4] Beijing National Laboratory for Condensed Matter Physics, Institute of Physics, Chinese Academy of Sciences, Beijing 100190, China. [5] Institute of Physical Science and Information Technology, Anhui University, Hefei 230601, China. [6] School of Chemical Engineering, Guangdong University of Petrochemical Technology, Maoming 525000, China. [7] These authors contributed equally: Xiaohui He, Qian He, Yuchen Deng. Correspondence and requests for materials should be addressed to D.M. (email: dma@pku.edu.cn) or to B.G. (email: bhge@iphy.ac.cn) or to H.J. (email: jihb@mail.sysu.edu.cn)

Single atom catalysts (SACs), with maximum atom-utilization and unique electronic and geometric properties[1], are becoming a thriving research field because of their enhanced catalytic performance in a wide scope of industrially important reactions, e.g., selective hydrogenation of nitroarenes, alkenes and carbonyl compounds[2–4], catalytic transformation of methane[5,6], aqueous reforming of methanol[7], hydroformylation of olefins[8], olefin metathesis[9], and oxygen reduction[10,11]. Various approaches have been utilized to prepare SACs, including the methods of impregnation/ion-exchange/co-precipitation[6,12,13], defect engineering[14], iced-photochemistry[15], atomic layer deposition[16,17], galvanic replacement[18], high-temperature migration[19], and high-temperature pyrolysis[20,21]. However, developing general protocols that can be used to easily synthesize of a wide variety of SACs is still highly desirable. For example, by Jung et al., theoretical calculations were conducted to predict universal principles for the electro-catalytic performance of SACs bearing various metal sites[22]. But the difficulty arises on verifying such predictions in experiments, as there are no general routes to prepare SACs with different center metals but similar supports and coordination environment. In addition, as predicted by Beller et al., the preparation of bi-/multi-metallic SACs is regarded as a next breakthrough because of their significant importance in the domino and tandem reactions[23], but there are few reports for their synthesis, mainly due to the huge obstacle to keep various metallic elements with obviously different physical/chemical properties coexisting in atomically dispersed states. Furthermore, comparative studies on the catalysis of different aggregation states, e.g., single atoms (SAs), nanoclusters (NCs), and nanoparticles (NPs), like the work by Zhang et al. on the Ru catalysts for CO_2 methanation[24], received extensive attention. But, most of these studies rely on tuning the aggregation states by changing the metal loadings[25,26], which did not conform to the single-factor-variable research method. Thus, a facile approach to regulate the aggregation states of metal species other than altering metal loading is desired.

Inspired by our previous work on the porous porphyrin polymers[27] and the work of Jiang et al. on SACs derived from metal-organic frameworks[21], we report here a precursor-dilution strategy to prepare N-doped porous carbon supported SACs. In brief, tetraphenylporphyrin (TPP) with chelated metal cations, acting as the metal precursor, is co-polymerized with excess amount of free TPP as the diluent. By the dilution, the mean distance between metal atoms dispersed on the as-prepared polymer matrix becomes sufficiently large, preventing their aggregation during the subsequent high-temperature pyrolysis. Thus, SACs are obtained. Specially, the high chelating ability of TPP to various metal cations[28–30] (Supplementary Fig. 1) empowers this method to be applicable for fabricating a wide variety of SACs. Using this strategy, we have successfully conducted the synthesis of 24 types of SACs (i.e., M_1/N–C, M = Ti, V, Cr, Mn, Fe, Co, Ni, Cu, Ga, Zr, Mo, Ru, Rh, Pd, Ag, Cd, In, Sn, Er, W, Ir, Pt, Au, and Bi), including noble metals and non-noble metals. Furthermore, by varying the preparation conditions, e.g., precursor concentrations, metal precursors, and pyrolysis temperatures, we can obtain various materials: SACs with different surface atom densities (0.002–0.034 Pt·nm^{-2}), bi-metallic SACs (Pt_1–Sn_1/N–C), and Pt catalysts with different aggregation states (Pt SAs, Pt NCs, and Pt NPs), respectively.

Results

Synthesis of Pt SACs with the precursor-dilution strategy. In this work, we use Pt_1/N–C as an example to show the precursor-dilution strategy for fabricating SACs (Fig. 1a). First, a mixture of tetraphenylporphyrin platinum (PtTPP) and free TPP (PtTPP:TPP = 1:40, mol:mol) was dissolved in dichloromethane, and then co-polymerized by the addition of anhydrous $AlCl_3$ (Friedel-Crafts alkylation reactions)[31]. The as-obtained polymers were treated at 600 °C under flowing N_2 gas, and nitrogen-doped-carbon supported Pt SACs (i.e., Pt_1/N–C) were obtained.

The transmission electron microscopy (TEM) image (Fig. 1b) and high-angle annular dark-field scanning transmission electron microscopy (STEM) image (Fig. 1c) revealed that there were no observable Pt NPs in the prepared SACs. The image taken by aberration corrected high-angle annular dark-field scanning transmission electron microscopy (AC HAADF-STEM) showed that individual Pt atoms highlighted by yellow circles in Fig. 1d were clearly visible (no bright dots can be observed in the underlying support of nitrogen-doped carbon without metal loading (i.e., N–C), Supplementary Fig. 2), resulting from the large difference in Z contrasts of the image for Pt and N/C. Thus, this image proved the presence of atomically dispersed Pt species. The X-ray diffraction (XRD) pattern of Pt_1/N–C exhibited no peaks at 39.8°, 46.2°, and 68.5° (Fig. 1e, PDF#04-0802). This pattern resembled that for N–C and indicated the highly dispersed state of Pt species. The aggregation state of Pt species was also probed by extended X-ray absorption fine structure spectrometry (EXAFS, Fig. 1f). There were two notable peaks at 1.7 and 2.5 Å, similar to those in the spectrum of PtTPP, which can be ascribed to the Pt–N and Pt–N–C contributions[32,33], respectively. It should be noted that the peak at 2.5 Å cannot be ascribed to the Pt–Pt bond (2.7 Å for Pt foil), which was further confirmed by the EXAFS fitting results of Pt_1/N–C (Supplementary Fig. 3, Supplementary Table 1). These fitting results were in good agreement with the original curves, and the coordination number of the Pt with surrounding N atoms was 3.4, indicating that the Pt atoms were connected with three or four N atoms[34,35]. These results again corroborated the dominant presence of atomically dispersed Pt species evidenced by AC HAADF-STEM. As shown from the X-ray absorption near edge structure (XANES) spectra (Supplementary Fig. 4), the energy absorption threshold of Pt_1/N–C located between Pt foil and PtO_2, implying the presence of positively charged $Pt^{\delta+}$ stabilized by adjacent N atoms in Pt_1/N–C. The oxidation state of Pt species was characterized by X-ray photoelectron spectroscopy (XPS, see Fig. 1g). The Pt 4*f* peaks located at 72.4 and 75.7 eV can be tentatively ascribed to Pt^{2+} with the presence of Pt–N bonds[36]. The inductively coupled plasma optical emission spectrometry (ICP-OES) analysis revealed that the actual Pt loading was 0.43 wt% (Supplementary Table 2), slightly lower than the nominal loading (0.73 wt%) estimated by the molar ratio of PtTPP:TPP (1:40). This may be caused by metal loss in the preparation process. The result of elemental analysis (EA) revealed 5.17 wt% nitrogen content of in Pt_1/N–C (Supplementary Table 2). High BET area (595 $m^2\,g^{-1}$) was found for Pt_1/N–C (Supplementary Table 2), and it was reported that high-surface-area structures could facilitate the atomic dispersion of metal species[37].

All the characterization results above lead to a conclusion that atomically dispersed Pt species were successfully synthesized on the support of N-doped carbon, by the precursor-dilution strategy. On the contrary, when PtTPP was used to make polymers without the diluent of free TPP, e.g., under the conditions of Pt–NPs/N–C(1:0), 100% PtTPP-based polymers and 3.31 wt% Pt loading (Supplementary Table 3), Pt NPs with 3.9 nm in diameter were formed using the same synthetic scheme (Supplementary Fig. 5). Thus, the diluent is indispensable for successful fabrication of SACs.

The versatility of the precursor-dilution strategy. The precursor-dilution strategy is of significant flexibility and

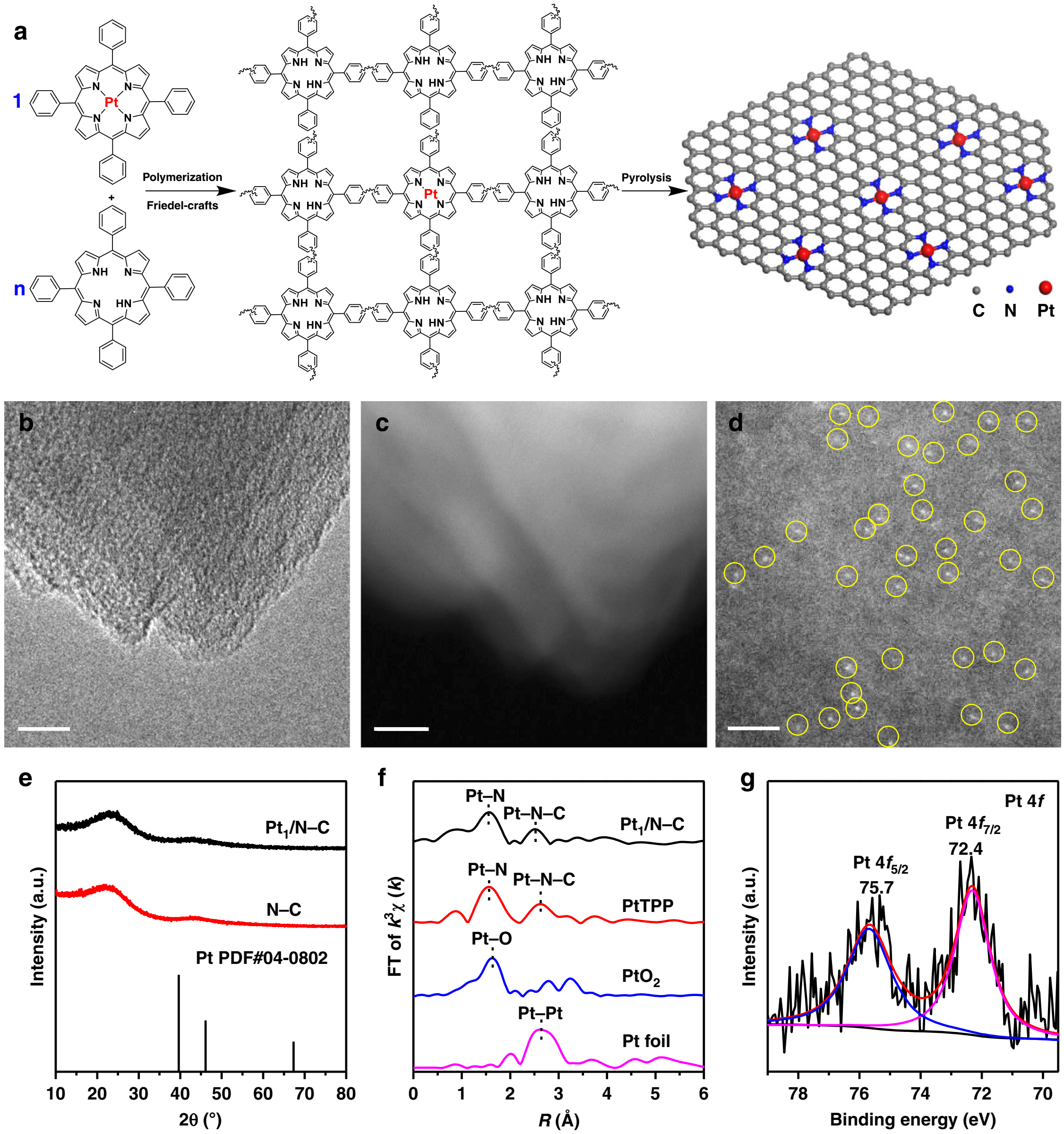

Fig. 1 Preparation and structural characterization of Pt_1/N-C. **a** Schematic illustration of the preparation of Pt_1/N-C. The molar ratio of PtTPP:TPP is denoted as 1:n. **b** TEM image of Pt_1/N-C. Scale bar, 10 nm. **c** STEM image of Pt_1/N-C. Scale bar, 10 nm. **d** AC HAADF-STEM image of Pt_1/N-C. SAs were highlighted by yellow circles. Scale bar, 2 nm. **e** XRD pattern of Pt_1/N-C and N-C. **f** The k^3-weighted R-space FT spectra of EXAFS for Pt_1/N-C, PtTPP, PtO_2, and Pt foil. **g** The XPS patterns of Pt 4*f* for Pt_1/N-C

generality for SAC fabrication, as demonstrated below. All of the synthesized catalysts were characterized fully by TEM, STEM, XRD, ICP-OES, EA, and BET (see Supplementary Figs. 6–28, 30–33 and Supplementary Tables 4–30). Among them, TEM/STEM images and XRD patterns were used to preliminarily identify the aggregation states of metal species on the supports. ICP-OES was used to reveal the content of metal species, and the EA and BET measurements were used to probe catalysts' texture.

First, we could extend the precursor-dilution strategy to fabricate a variety of SACs using MTPP with different metals (M = Ti, V, Cr, Mn, Fe, Co, Ni, Cu, Ga, Zr, Mo, Ru, Rh, Pd, Ag, Cd, In, Sn, Er, W, Ir, Au, and Bi) as the precursors and free TPP as the diluent. For most of the metals, the ratio of MTPP:TPP of 1:40 was used during the catalyst synthesis. But, there were exceptions. Some MTPPs (e.g., MnTPP and FeTPP) were found to easily leach in the polymerization process (under 80 °C and in $AlCl_3$). Thus, the molar ratios of MTPP:TPP were increased to obtain SACs with meaningful metal loadings (>0.05 wt%). The samples with high content of Rh or Au tended to form NPs, so the molar ratios of RhTPP:TPP and AuTPP:TPP were decreased to 1:80 and 1:160, respectively, in order to obtain atomically dispersed metal species. Details of all the synthesis were provided in Supplementary Methods. AC HAADF-STEM images (Fig. 2) showed that all of the 24 SACs featured with atomically dispersed species on the supports, which were further confirmed by the corresponding EXAFS results with the absence of metal–metal bond (Supplementary Fig. 29). Among them, SACs of Cd, Bi, and Er have never been reported before, which may underpin the exploration of intriguing applications[38]. The EA and BET results revealed some similarity of material texture among all of the catalysts, i.e., with >420 $m^2\,g^{-1}$ BET areas and ~5.0 wt% nitrogen content, due to the utilization of the similar preparation protocols.

Second, we could tune the surface Pt atom density in Pt_1/N–C by changing the precursor concentrations (i.e., the molar ratios of

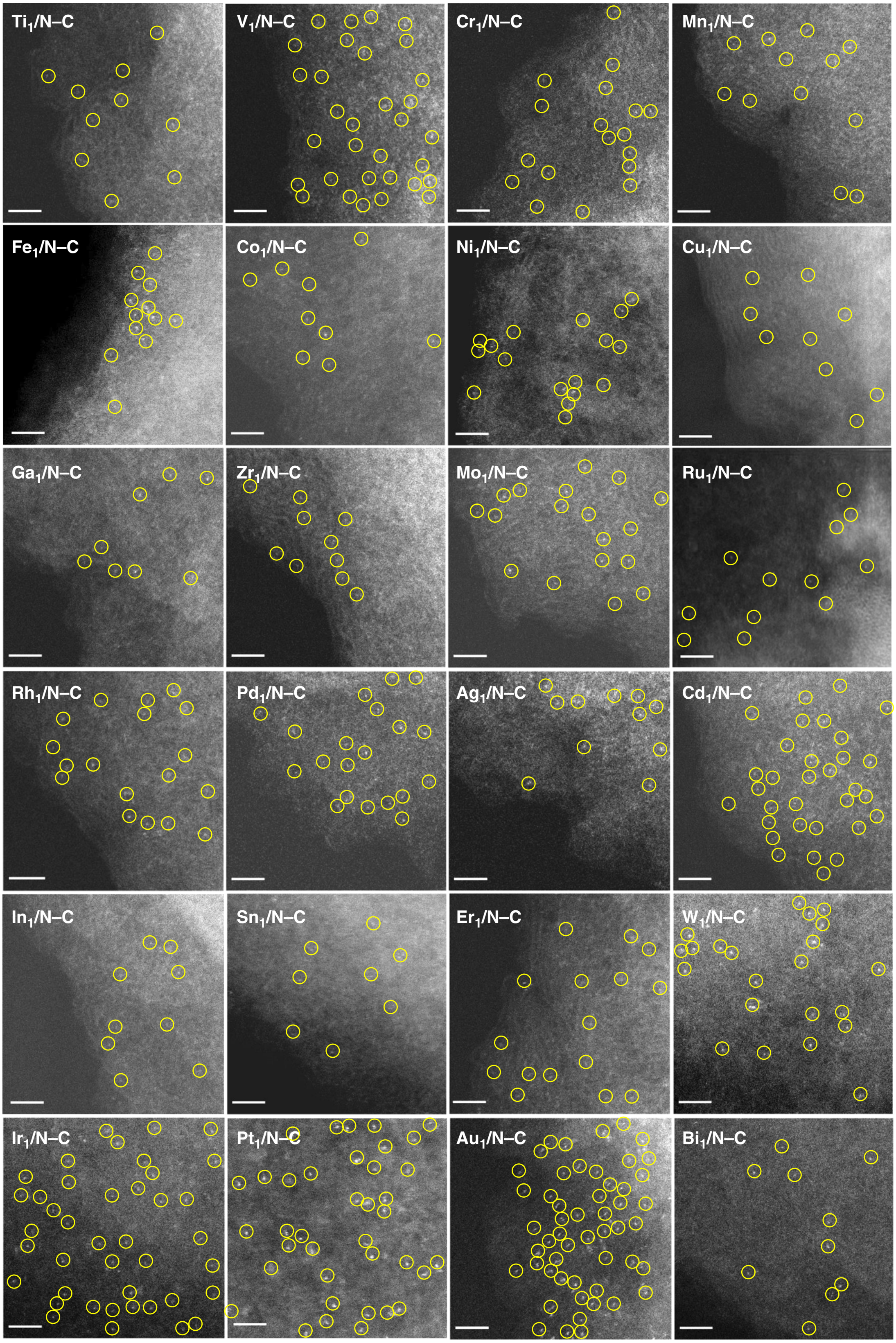

Fig. 2 AC HAADF-STEM images of M_1/N-C. M = Ti, V, Cr, Mn, Fe, Co, Ni, Cu, Ga, Zr, Mo, Ru, Rh, Pd, Ag, Cd, In, Sn, W, Ir, Pt, Au, and Bi. SAs were highlighted by yellow circles. Scale bar, 2 nm

PtTPP:TPP). Using different molar ratios of PtTPP:TPP (i.e., 1:320, 1:80, 1:40, and 1:20), we prepared a set of SACs with different Pt contents (0.06, 0.21, 0.43, and 0.73 wt%, respectively) and similar BET areas (~600 $m^2 g^{-1}$, see Supplementary Tables 2 and 27–29), and thus different Pt surface densities (0.002, 0.010, 0.022, and 0.034 Pt·nm^{-2}, respectively)[39,40], in line with the trend observed by AC HAADF-STEM (Fig. 3).

Third, fabricating bi-metallic SACs (e.g., Pt_1–Sn_1/N–C) was also achieved with the same synthesis procedure of Pt_1/N–C and the precursor molar ratio of PtTPP:SnTPP:TPP (1:1:40). The N-doped porous carbon-based materials with 0.48 wt% Pt loading and 0.35 wt% Sn loading were obtained (Supplementary Table 30). This ratio of Pt loading and Sn loading (1.4:1) was in good agreement with the nominal ratio (1.6:1), based on the molar ratio of PtTPP:SnTPP (1:1) and atomic weight ratio of Pt:Sn (195.1:118.7). The AC HAADF-STEM image for Pt_1–Sn_1/N–C revealed the metal species atomically dispersed on the porous carbon supports (Fig. 4a). Corresponding element mapping analysis of Pt_1–Sn_1/N–C revealed that both Pt and Sn species were homogeneously distributed (Fig. 4b). The results of EXAFS (no Pt–Pt bond and Sn–Sn bond, Fig. 4c, d) were also indicative of the dominant presence of isolated Pt and Sn atoms deposited on the carbon matrix. These mutually authenticated results provided compelling evidence for the preparation of Pt_1–Sn_1/N–C.

Forth, we found that the pyrolysis temperature during the materials fabrication could influence the aggregation states of dispersed metal atoms. When the samples with the same molar ratio of PtTPP:TPP (1:40) were treated in different pyrolysis temperatures (i.e., 600, 700, and 800 °C), the Pt contents and BET surface areas of them were close (~0.5 wt% and ~600 $m^2 g^{-1}$, respectively, see Supplementary Tables 2 and 31–32), while the aggregation states of Pt species were changed from SAs (Pt_1/N–C) to NCs (Pt–NCs/N–C, 1.1 nm) and NPs (Pt–NPs/N–C, 6.9 nm) (Fig. 1d, Fig. 5 and Supplementary Figs. 34–35).

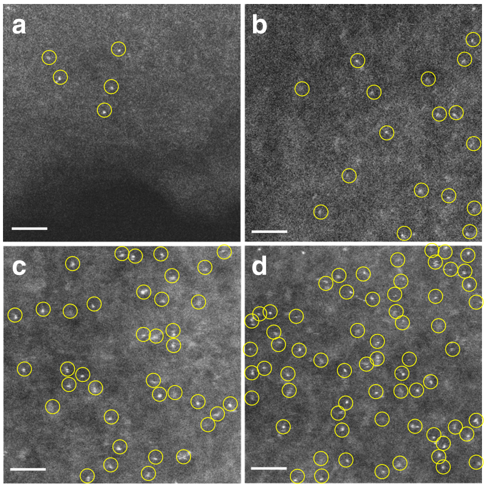

Fig. 3 AC HAADF-STEM images of Pt SACs with different atom densities. AC HAADF-STEM images of **a** Pt_1/N-C(1:320); **b** Pt_1/N-C(1:80); **c** Pt_1/N-C (1:40); and **d** Pt_1/N-C(1: 20). SAs are highlighted by yellow circles. Scale bar, 2 nm

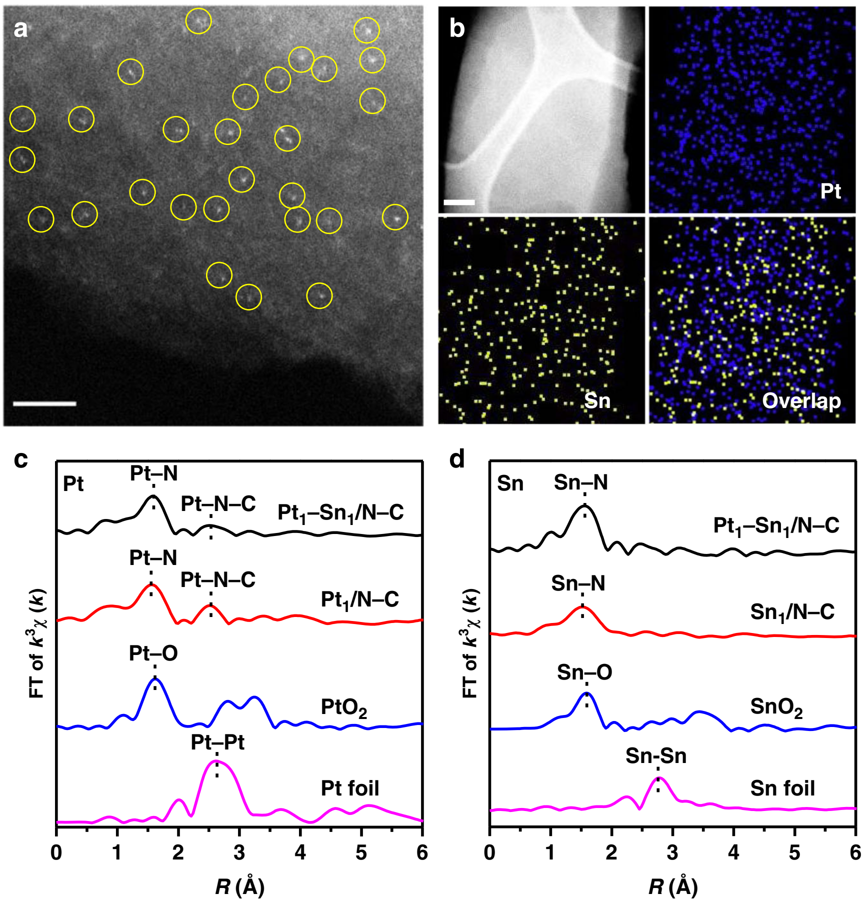

Fig. 4 Structural characterization of Pt_1–Sn_1/N-C. **a** AC HAADF-STEM image of Pt_1–Sn_1/N-C. SAs were highlighted by yellow circles. Scale bar, 2 nm. **b** element mapping of Pt_1–Sn_1/N-C. Scale bar, 100 nm. **c** The Pt k^3-weighted R-space FT spectra of EXAFS for Pt_1–Sn_1/N-C, Pt_1/N-C, PtO_2, and Pt foil. **d** The Sn k^2-weighted R-space FT spectra of EXAFS for Pt_1–Sn_1/N-C, Sn_1/N-C, SnO_2, and Sn foil

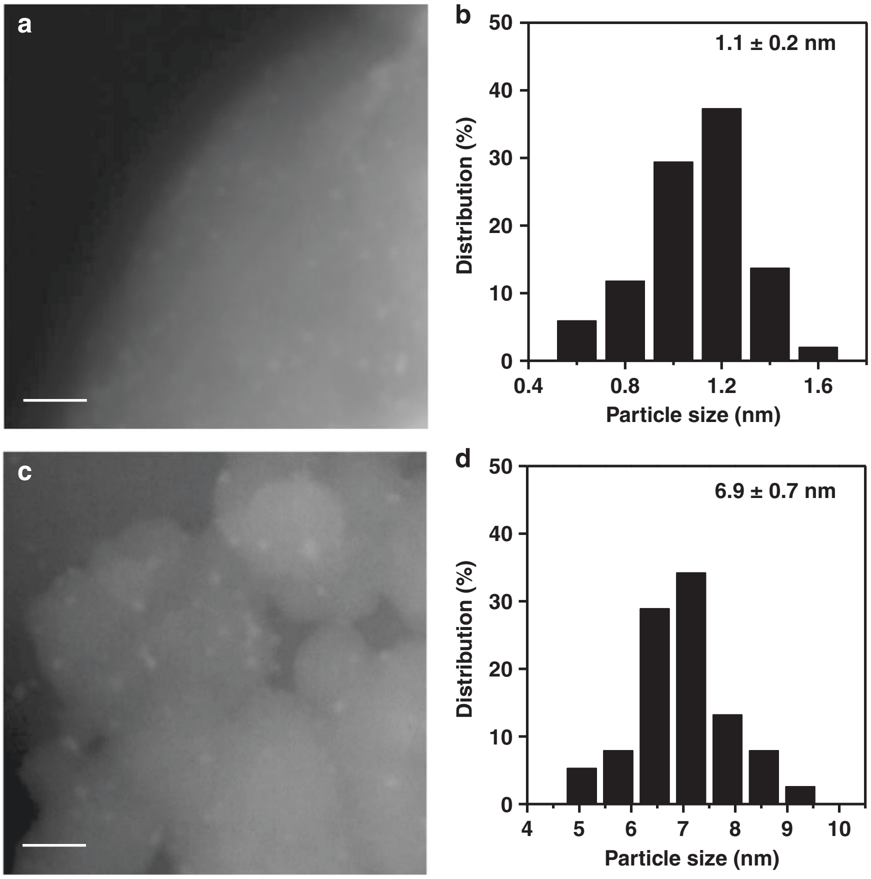

Fig. 5 Structural characterization of Pt-NCs/N-C and Pt-NPs/N-C. **a** STEM image of Pt-NCs/N-C. Scale bar, 10 nm. **b** Particle size distribution of Pt-NCs/N-C. **c** STEM image of Pt-NPs/N-C. Scale bar, 50 nm. **d** Particle size distribution of Pt-NPs/N-C

The chemo-/regio-selectivity of Pt SACs in hydrogenation. After illustrating the facile synthetic routes of SACs with great versatility, we show here the unique catalytic properties of SACs (Pt_1/N–C, with 0.43 wt% Pt loading) compared with NPs (Pt–NPs/N–C, with Pt–NPs of 6.9 nm in diameter and 0.52 wt% Pt loading) in hydrogenation reactions, which were previously illustrated as a promising solution in practical applications of SACs[1]. To our great delight, Pt_1/N–C showed excellent chemoselectivity in the hydrogenation of 1-nitro-4-ethynylbenzene (with –C≡CH and $–NO_2$) and 1-ethynyl-4-vinylbenzene (with –C≡CH and $–C{=}CH_2$), as it only transformed alkyne groups to alkenyl groups and kept $–NO_2$ and $–C{=}CH_2$ intact (99% selectivity to 1-nitro-4-vinylbenzene and 99% selectivity to 1,4-divinylbenzene at ~20% conversion level, and 98% selectivity to 1-nitro-4-vinylbenzene and 97% selectivity to 1,4-divinylbenzene at ~100% conversion level, respectively, Fig. 6a, b and Supplementary Fig. 36a, b). In contrast, similar catalysis on Pt–NPs/N–C induced the formation of multiple products, resulting from the co-hydrogenation of –C≡CH and $–NO_2$, and –C≡CH and –C=C, respectively. The Pt_1/N–C catalyst permits the distinction between –C≡CH and $–NO_2$/–C=C in hydrogenation mainly because of the good match between the relatively low catalytic activity of Pt SACs and high reactivity of terminal alkynes[41].

More inspiringly, our Pt_1/N–C showed rarely reported regioselectivity in the hydrogenation of 1-ethynyl-4-(phenylethynyl)benzene and 1-(dec-1-yn-1-yl)-3-ethynylbenzene (with –C≡CH and –C≡C–), as it only converted terminal alkyne to alkenyl while kept internal alkyne intact: 99% selectivity to 1-(phenylethynyl)-4-vinylbenzene and 99% selectivity to 1-(dec-1-yn-1-yl)-3-vinylbenzene at ~20% conversion level, and 98% selectivity to 1-(phenylethynyl)-4-vinylbenzene and 97% selectivity to 1-(dec-1-yn-1-yl)-3-vinylbenzene at ~100% conversion level, respectively (Fig. 6c, d, Supplementary Figs. 36c and 36d). However, similar hydrogenation reactions catalyzed by Pt–NPs/N–C were not selective, i.e., both terminal and internal alkynes were hydrogenated. For example, the hydrogenation of 1-ethynyl-4-(phenylethynyl)benzene catalyzed by Pt–NPs/N–C showed 13%, 12%, and 75% selectivities to 1-(phenylethynyl)-4-vinylbenzene, 1-ethyl-4-(phenylethynyl)benzene, and 1-styryl-4-vinylbenzene, respectively (Fig. 6c).

It is generally accepted that there are two activation pathways for semi-hydrogenation of alkyne: (i) the terminal of the –C≡CH group interacts with metal surfaces leading to deprotonation, and then the –C≡C group becomes activated; (ii) the entire –C≡C group interacts with the metal surfaces and becomes activated[42]. In our system, because of possible steric hindrance effect (1.2 Å for C≡C bond length vs. 0.8 Å for Pt^{2+} radius[43]) of Pt_1/N–C, the first pathway is more probable. Apparently, due to its absence of terminal hydrogen, internal alkyne cannot be activated and then hydrogenated on Pt_1/N–C. On the contrary, Pt–NPs/N–C with much larger diameters than that of Pt_1/N–C are able to interact with substrates with less steric hindrance effect[44] and then catalyze the hydrogenation of both terminal and internal alkynes. To verify our assumption, Pt_1/N–C, Pt–NCs/N–C (1.1 nm), and Pt–NPs/N–C (6.9 nm) were employed under the same reaction conditions (Supplementary Table 33). As expected, the catalytic activities (i.e., turnover frequency, TOF, based on the metal dispersion[13]) for the hydrogenation of internal alkynes on Pt–NCs/N–C fell between those on Pt_1/N–C and Pt–NPs/N–C: 1-phenyl-1-propyne (0, 132, and 2946 h^{-1}), 1-phenyl-1-pentyne (0, 93, and 2556 h^{-1}), and 5-decyne (0, 2860, and 13300 h^{-1}) on SACs, NCs, and NPs, respectively. The observation that the

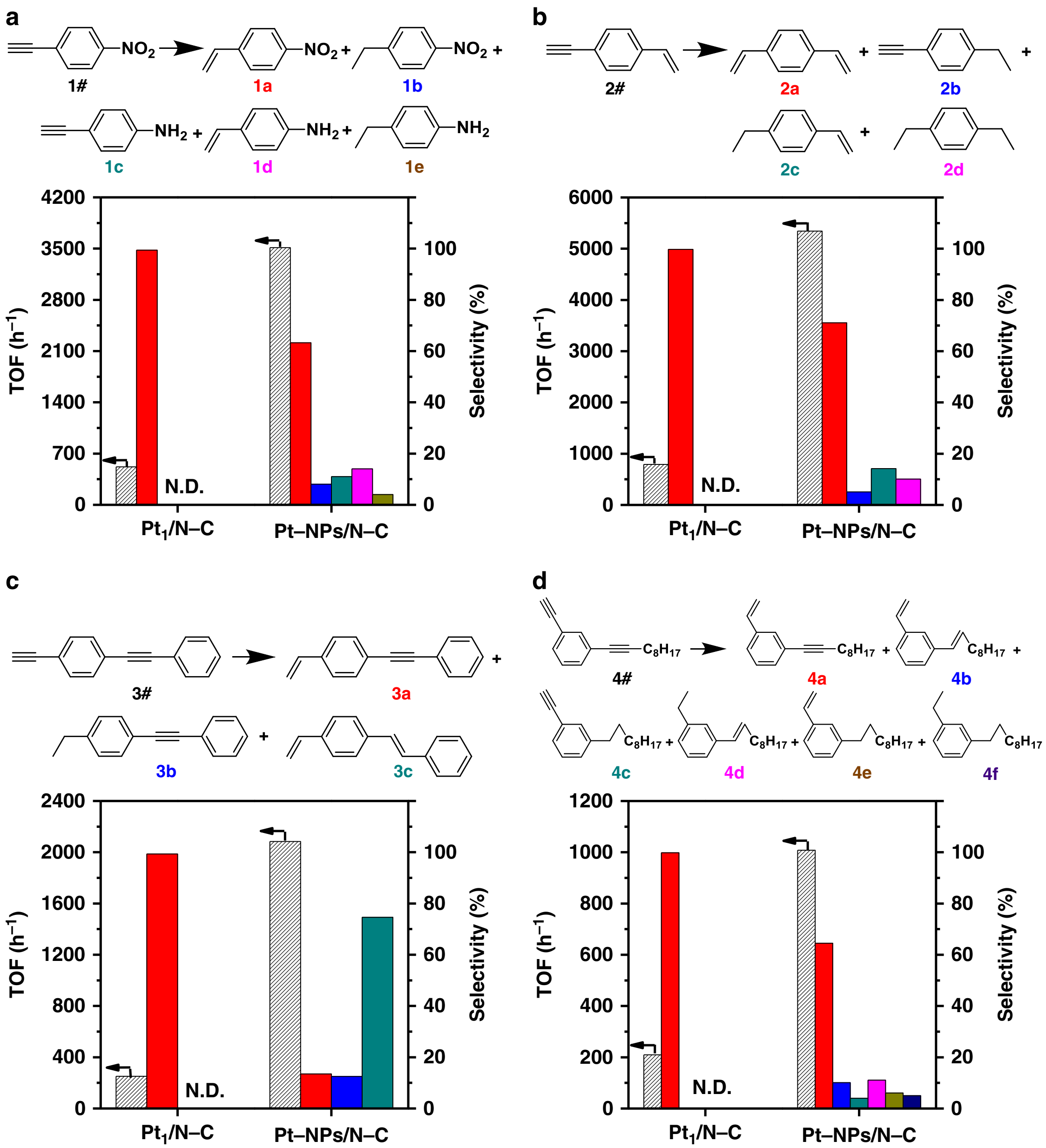

Fig. 6 Catalytic performance of Pt_1/N-C and Pt-NPs/N-C. Reaction results for the hydrogenation of **a** 1-nitro-4-ethynylbenzene, **b** 1-ethynyl-4-vinylbenzene, **c** 1-ethynyl-4-(phenylethynyl)benzene, **d** 1-(dec-1-yn-1-yl)-3-ethynylbenzene on Pt_1/N-C and Pt-NPs/N-C. Reaction condition: substrate (0.5 mmol), catalyst (Pt:substrate = 1:1200, mol:mol), methanol (2.0 mL), H_2 (1.0 MPa), 50 °C (**a**, **b**) or 80 °C (**c**, **d**). All the conversions were maintained at ~20%. TOF was calculated based on Pt dispersion (Pt_1/N-C: 100%; Pt-NPs/N-C: 14.5%, estimated by particle size (6.9 nm) according to $D = 1/d_{Pt}$)

activities for the hydrogenation of internal alkynes increased with the increasing size of Pt species coincided quite well with our speculation that the unique group discrimination of terminal alkynes from internal ones on Pt_1/N–C can be attributed to the geometric effect (see Supplementary Fig. 37).

In addition, the stability of the Pt_1/N–C catalysts in the hydrogenation of the four substrates, i.e., 1-nitro-4-ethynylbenzene, 1-ethynyl-4-vinylbenzene, 1-ethynyl-4-(phenylethynyl)benzene, and 1-(dec-1-yn-1-yl)-3-ethynylbenzene, respectively, was evaluated. As shown in Supplementary Fig. 38, recycling Pt_1/N–C catalysts for five runs exhibited no essential decrease in catalytic activities and selectivities (~98%). Furthermore, no Pt nanoparticles or nanoclusters were found in TEM and STEM images (Supplementary Fig. 39), and the corresponding AC HAADF-STEM images revealed that the Pt species maintained the atomically dispersed states after five catalytic runs. These results above suggested that the Pt_1/N–C catalysts exhibited excellent recyclability under the aforementioned reaction conditions.

Discussion

In summary, a precursor-dilution strategy was developed to synthesize a series of SACs on N-doped porous carbon supports. This strategy is facile and versatile, and thus meets the requirements of the in-depth research nowadays. The Pt_1/N–C SACs prepared with this strategy showed extremely high chemo- and regioselectivity towards terminal alkynes in hydrogenation. These findings are of significant importance in broadening the application of SACs, with the implication that SACs are able to achieve superior selectivity comparable to homogeneous catalysts and enzyme catalysts, for the catalysis of complex molecules.

Methods

Catalyst preparation. Take Pt_1/N–C as example. Under a nitrogen atmosphere, 100 mL stainless batch tank reactor was charged with a solution of PtTPP (0.038 mmol), TPP (1.500 mmol), and anhydrous $AlCl_3$ (24 mmol) in 30 mL of dichloromethane (PtTPP:TPP = 1:40, mol:mol). The reaction mixture was stirred at 80 °C for 24 h and then cooled to room temperature. The as-obtained precipitate was filtered and washed with methanol, dichloromethane, tetrahydrofuran, N,N-dimethylformamide, and acetone, respectively. Subsequently, the resulted polymer was further purified by Soxhlet extractions for 24 h with methanol and dichloromethane, respectively. After dried at 80 °C in vacuum for 24 h, the polymer was placed in a tube furnace, heated to 600 °C for 3 h at the heating rate of 5 °C min^{-1} under flowing nitrogen gas and then naturally cooled to room temperature to obtain Pt_1/N–C. Detailed preparation conditions for other samples were described in Supplementary Methods.

Characterization. EA and ICP-OES were performed on Vario EL cube instrument and PerkinElmer OPTIMA 8000DV, respectively. BET surface areas measurements were performed on a Micromeritic ASAP2020M analyzer at liquid nitrogen temperature. Before the measurement, samples were evacuated at 200 °C for 6 h. Specific surface areas were calculated based on the BET equation. The Pt surface density was calculated by the equation: Pt surface density = [Pt loading] × N_A/(195.08 × [surface area]), where N_A is the Avogadro's number, and Pt loading and the surface area were obtained by the measurement of ICP-OES and BET, respectively. XRD patterns were obtained on a Bruker D8 Advanced diffractometer in the 2θ range 10–80°. XPS measurements were performed on an ESCALab250 XPS system with Al Kα source and a charge neutralizer, and the binding energies were referenced to the contaminated C 1*s* (284.8 eV). TEM images and STEM images were obtained on FEI Tecnai G2 F30 operated at 300 kV. AC HAADF-STEM images were obtained on a JEM-ARM200F transmission electron microscopy operated at 200 kV, which incorporated with double spherical aberration correctors. X-ray absorption spectroscopy (XAS) measurements were conducted on BL14W beamline at the Shanghai Synchrotron Radiation Facility (SSRF) and 1W1B beamline at the Beijing Synchrotron Radiation Facility (BSRF). The sample of SACs were measured in fluorescence mode using Lytle detector or 32-element Ge solid state detector and the corresponding metal foils and metal oxides were used as reference samples and measured in the transmission mode. ^1H and ^{13}C nuclear magnetic resonance (NMR) spectrums were obtained on Bruker Avance III 500 HD. High-resolution mass spectral (HRMS) data were obtained on Thermo Fisher Scientific Tribrid Mass Spectrometer (Orbitap Fusion Lumos).

Catalytic performance test. Catalytic hydrogenation reactions of various substrates, including 1-phenyl-1-propyne, 1-phenyl-1-pentyne, 5-decyne, 1-nitro-4-ethynylbenzene, 1-ethynyl-4-vinylbenzene, 1-ethynyl-4-(phenylethynyl)benzene, and 1-(dec-1-yn-1-yl)-3-ethynylbenzene, were carried out in 10 mL stainless autoclave. Take hydrogenation of 1-nitro-4-ethynylbenzene on Pt_1/N–C as example. The typical reaction conditions were 0.5 mmol 1-nitro-4-ethynylbenzene, 20 mg Pt_1/N–C catalyst (0.43 wt%, Pt:1-nitro-4-ethynylbenzene = 1:1200, mol: mol), 2.0 mL methanol as solvent, 1.0 MPa H_2 and 50 °C. After cooled and filtered, the reaction products were analyzed by GC (Shimadzu 2010 GC Plus) and GC-MS (Shimadzu GCMS-QP2010 Ultra). Selectivities were reported on a carbon basis, and TOF as molar substrate conversion rates per mole of surface Pt atoms per hour (h^{-1}). For Pt_1/N–C, the Pt dispersion was estimated to be 100%; for Pt–NCs and Pt–NPs, the dispersion (D) was estimated by the metal particle size (d) according to $D = 1/d_{pt}$, respectively. Detailed reaction conditions were given in the footnotes of Fig. 6 and Supplementary Table 33. Corresponding ^1H and ^{13}C NMR spectrums of some uncommon substrates and products, including 1-ethynyl-4-(phenylethynyl) benzene (3#), 1-(phenylethynyl)-4-vinylbenzene (3a), 1-ethyl-4-(phenylethynyl) benzene (3b), 1-styryl-4-vinylbenzene (3c), 1-(dec-1-yn-1-yl)-3-ethynylbenzene (4#), 1-(dec-1-yn-1-yl)-3-vinylbenzene (4a), 1-(dec-1-en-1-yl)-3-vinylbenzene (4b), 1-decyl-3-ethynylbenzene (4c), 1-(dec-1-en-1-yl)-3-ethylbenzene (4d), 1-decyl-3-vinylbenzene (4e), and 1-decyl-3-ethylbenzene (4f) were showed in Supplementary Figs. 40–61, respectively.

Data availability

The data underlying Figs. 1 and 4–6, Supplementary Figs. 3–36 and 38 are provided as a Source Data file. The other data that support the findings of this study are available from the corresponding author upon request.

Received: 24 January 2019 Accepted: 25 July 2019
Published online: 14 August 2019

References

1. Wang, A., Li, J. & Zhang, T. Heterogeneous single-atom catalysis. *Nat. Rev. Chem.* **2**, 65–81 (2018).
2. Yan, H. et al. Atomic engineering of high-density isolated Co atoms on graphene with proximal-atom controlled reaction selectivity. *Nat. Commun.* **9**, 3197 (2018).
3. Wei, H. et al. FeO_x-supported platinum single-atom and pseudo-single-atom catalysts for chemoselective hydrogenation of functionalized nitroarenes. *Nat. Commun.* **5**, 5634 (2014).
4. Zhang, B. et al. Stabilizing a $platinum_1$ single-atom catalyst on supported phosphomolybdic acid without compromising hydrogenation activity. *Angew. Chem. Int. Ed.* **55**, 8319–8323 (2016).
5. Guo, X. et al. Direct, nonoxidative conversion of methane to ethylene, aromatics, and hydrogen. *Science* **344**, 616–619 (2014).
6. Shan, J. et al. Mild oxidation of methane to methanol or acetic acid on supported isolated rhodium catalysts. *Nature* **551**, 605–608 (2017).
7. Lin, L. et al. Low-temperature hydrogen production from water and methanol using Pt/alpha-MoC catalysts. *Nature* **544**, 80–83 (2017).
8. Lang, R. et al. Hydroformylation of olefins by a rhodium single-atom catalyst with activity comparable to $RhCl(PPh_3)_3$. *Angew. Chem. Int. Ed.* **55**, 16054–16058 (2016).
9. Zhao, P. et al. Entrapped single tungstate site in zeolite for cooperative catalysis of olefin metathesis with bronsted acid site. *J. Am. Chem. Soc.* **140**, 6661–6667 (2018).
10. Yin, P. et al. Single cobalt atoms with precise N-Coordination as superior oxygen reduction reaction catalysts. *Angew. Chem. Int. Ed.* **55**, 10800–10805 (2016).
11. Chen, Y. et al. Enhanced oxygen reduction with single-atomic-site iron catalysts for a zinc-air battery and hydrogen-air fuel cell. *Nat. Commun.* **9**, 5422 (2018).
12. Zhao, C. et al. Ionic exchange of metal organic frameworks to access single nickel sites for efficient electroreduction of CO_2. *J. Am. Chem. Soc.* **139**, 8078–8081 (2017).
13. Qiao, B. et al. Single-atom catalysis of CO oxidation using Pt_1/FeO_x. *Nat. Chem.* **3**, 634–641 (2011).
14. Wan, J. et al. Defect effects on TiO_2 nanosheets: stabilizing single atomic site Au and promoting catalytic properties. *Adv. Mater.* **30**, 1705369 (2018).
15. Wei, H. et al. Iced photochemical reduction to synthesize atomically dispersed metals by suppressing nanocrystal growth. *Nat. Commun.* **8**, 1490 (2017).
16. Sun, S. H. et al. Single-atom catalysis using Pt/graphene achieved through atomic layer deposition. *Sci. Rep.* **3**, 1775 (2013).
17. Liu, S. et al. Stabilizing single-atom and small-domain platinum via combining organometallic chemisorption and atomic layer deposition. *Organometallics* **36**, 818–828 (2017).
18. Lucci, F. R. et al. Selective hydrogenation of 1,3-butadiene on platinum-copper alloys at the single-atom limit. *Nat. Commun.* **6**, 8550 (2015).
19. Jones, J. et al. Thermally stable single-atom platinum-on-ceria catalysts via atom trapping. *Science* **353**, 150–154 (2016).
20. Chen, Y. et al. Isolated single iron atoms anchored on N-doped porous carbon as an efficient electrocatalyst for the oxygen reduction reaction. *Angew. Chem. Int. Ed.* **56**, 6937–6941 (2017).
21. Jiao, L. et al. From metal-organic frameworks to single-atom Fe implanted N-doped porous carbons: Efficient oxygen reduction in both alkaline and acidic media. *Angew. Chem. Int. Ed.* **57**, 8525–8529 (2018).
22. Back, S. et al. Single-atom catalysts for CO_2 electroreduction with significant activity and selectivity improvements. *Chem. Sci.* **8**, 1090–1096 (2017).
23. Cui, X. et al. Bridging homogeneous and heterogeneous catalysis by heterogeneous single-metal-site catalysts. *Nat. Catal.* **1**, 385–397 (2018).
24. Guo, Y. et al. Low-temperature CO_2 methanation over CeO_2-supported Ru single atoms, nanoclusters, and nanoparticles competitively tuned by strong metal–support interactions and H-spillover effect. *ACS Catal.* **8**, 6203–6215 (2018).
25. Chen, Y. et al. Identifying size effects of Pt as single atoms and nanoparticles supported on FeO_x for the water-gas shift reaction. *ACS Catal.* **8**, 859–868 (2018).
26. Caparrós, F. J. et al. Remarkable carbon dioxide hydrogenation to ethanol on a palladium/iron oxide single-atom catalyst. *ChemCatChem* **10**, 2365–2369 (2018).
27. Chen, Y. et al. State-of-the-art aluminum porphyrin-based heterogeneous catalysts for the chemical fixation of CO_2 into cyclic carbonates at ambient conditions. *ChemCatChem* **9**, 767–773 (2017).
28. Sun, E.-j et al. Synthesis and properties of 5,10,15,20-tetra(4-lauroylimidophenyl)porphyrin and its metal complexes. *Solid State Sci.* **9**, 1061–1068 (2007).
29. Stangel, C. et al. Noble metal porphyrin derivatives bearing carboxylic groups: synthesis, characterization and photophysical study. *Polyhedron* **52**, 1016–1023 (2013).
30. Santria, A., Fuyuhiro, A., Fukuda, T. & Ishikawa, N. Synthesis of a series of heavy lanthanide(III) monoporphyrinato complexes with tetragonal symmetry. *Inorg. Chem.* **56**, 10625–10632 (2017).

31. Wang, S. et al. A novel metalporphyrin-based microporous organic polymer with high CO_2 uptake and efficient chemical conversion of CO_2 under ambient conditions. *J. Mater. Chem. A* **5**, 1509–1515 (2017).
32. Obata, M. et al. Synthesis of poly(isobutyl-co-2,2,2-trifluoroethyl methacrylate) with 5,10,15,20-tetraphenylporphinato platinum(II) moiety as an oxygen-sensing dye for pressure-sensitive paint. *J. Polym. Sci. Pol. Chem.* **43**, 2997–3006 (2005).
33. Liu, J. et al. High performance platinum single atom electrocatalyst for oxygen reduction reaction. *Nat. Commun.* **8**, 15938 (2017).
34. Li, T., Liu, J., Song, Y. & Wang, F. Photochemical solid-phase synthesis of platinum single atoms on nitrogen-doped carbon with high loading as bifunctional catalysts for hydrogen evolution and oxygen reduction reactions. *ACS Catal.* **8**, 8450–8458 (2018).
35. He, T. et al. Zirconium-porphyrin-based metal-organic framework hollow nanotubes for immobilization of noble-metal single atoms. *Angew. Chem. Int. Ed.* **57**, 3493–3498 (2018).
36. Ou, M. et al. Single Pt atoms deposition on g-C_3N_4 nanosheets for photocatalytic H_2 evolution or NO oxidation under visible light. *Int. J. Hydrog. Energy* **42**, 27043–27054 (2017).
37. Guan, Y. et al. Ganoderma-like MoS_2/NiS_2 with single platinum atoms doping as an efficient and stable hydrogen evolution reaction catalyst. *Small* **14**, 1800697 (2018).
38. Li, Z., Wang, D., Wu, Y. & Li, Y. Recent advances in the precise control of isolated single-site catalysts by chemical methods. *Natl. Sci. Rev.* **5**, 673–689 (2018).
39. Duan, S., Wang, R. & Liu, J. Stability investigation of a high number density Pt_1/Fe_2O_3 single-atom catalyst under different gas environments by HAADF-STEM. *Nanotechnology* **29**, 204002 (2018).
40. Kunwar, D. et al. Stabilizing high metal loadings of thermally stable platinum single atoms on an industrial catalyst support. *ACS Catal.* **9**, 3978–3990 (2019).
41. Yabe, Y., Sawama, Y., Monguchi, Y. & Sajiki, H. New aspect of chemoselective hydrogenation utilizing heterogeneous palladium catalysts supported by nitrogen- and oxygen-containing macromolecules. *Catal. Sci. Technol.* **4**, 260–271 (2014).
42. Li, G. & Jin, R. Gold nanocluster-catalyzed semihydrogenation: a unique activation pathway for terminal alkynes. *J. Am. Chem. Soc.* **136**, 11347–11354 (2014).
43. Ahrens, L. H. The use of ionization potentials Part 1. Ionic radii of the elements. *Geochim. Cosmochim. Acta* **2**, 155–169 (1952).
44. Yan, H. et al. Single-atom Pd_1/graphene catalyst achieved by atomic layer deposition: Remarkable performance in selective hydrogenation of 1,3-butadiene. *J. Am. Chem. Soc.* **137**, 10484–10487 (2015).

Acknowledgements

This work was supported by the National Natural Science Foundation of China (Nos. 21606260, 21576302, 21376278, 21725301, 21821004, and 91645115), the National Science Foundation for Distinguished Young Scholars of China (No. 21425627), the NSF of Guangdong Province (2015A030313104), the Fundamental Research Funds for the Central Universities of Sun Yat-sen University (15lgjc33, 16lgpy15), the National Key R&D Program of China (2017YFB0602200), the Features Innovative Projects of Department of Education of Guangdong Province (No. 2016KTSCX003), and Local Innovative and Research Teams Project of Guangdong Pearl Rivers Talents Program (2017BT01C102).

Author contributions

X.H., Q.H. and Y.D. equally contributed to this work. X.H. developed the concept, designed these experiments, and analyzed experimental data. Q.H., H.C. and Y.Z. contributed to catalyst synthesis and catalytic experiments. Y.D., M.P., S.Y., M.Z. and D.M. performed the EXAFS measurements and analyzed the data. B.G. collected and analyzed the AC HAADF-STEM data. X.H., Q.H., D.X. and D.M. wrote the paper. D.M. and H.J. directed the project. All authors discussed the results and commented on the paper.

Additional information

Supplementary Information accompanies this paper at https://doi.org/10.1038/s41467-019-11619-6.

Competing interests: The authors declare no competing interests.

Reprints and permission information is available online at http://npg.nature.com/reprintsandpermissions/

Peer review information: *Nature Communications* thanks Abhaya Datye, and the other, anonymous, reviewer(s) for their contribution to the peer review of this work. Peer reviewer reports are available.

Publisher's note: Springer Nature remains neutral with regard to jurisdictional claims in published maps and institutional affiliations.